Journal of
Marine Science
and Engineering

Article

Terminal Phase Navigation for AUV Docking: An Innovative Electromagnetic Approach

Yevgeni Gutnik * and Morel Groper

The Hatter Department of Marine Technologies, Leon H. Charney School of Marine Sciences, University of Haifa, 199 Aba Khoushy Ave., Mount Carmel, Haifa 3498838, Israel; mgroper@univ.haifa.ac.il
* Correspondence: ygutnik@campus.haifa.ac.il

Featured Application: Precise close range underwater electromagnetic navigation and docking.

Abstract: This study introduces a groundbreaking approach for real-time 3D localization, specifically focusing on achieving seamless and precise localization during the terminal guidance phase of an autonomous underwater vehicle (AUV) as it approaches an omnidirectional docking component in an automated deployable launch and recovery system (LARS). Using the AUV's magnetometer, an economical electromagnetic beacon embedded in the docking component, and an advanced signal processing algorithm, this novel approach ensures the accurate localization of the docking component in three dimensions without the need for direct line-of-sight contact. The method's real-time capabilities were rigorously evaluated via simulations, prototype experiments in a controlled lab setting, and extensive full-scale pool experiments. These assessments consistently demonstrated an exceptional average positioning accuracy of under 3 cm, marking a significant advancement in AUV guidance systems.

Keywords: AUV navigation; electromagnetic guidance; launch and recovery; magnetometer; underwater docking

Citation: Gutnik, Y.; Groper, M. Terminal Phase Navigation for AUV Docking: An Innovative Electromagnetic Approach. *J. Mar. Sci. Eng.* **2024**, *12*, 192. https://doi.org/10.3390/jmse12010192

Academic Editor: Weicheng Cui

Received: 3 December 2023
Revised: 17 January 2024
Accepted: 18 January 2024
Published: 21 January 2024

Copyright: © 2024 by the authors. Licensee MDPI, Basel, Switzerland. This article is an open access article distributed under the terms and conditions of the Creative Commons Attribution (CC BY) license (https://creativecommons.org/licenses/by/4.0/).

1. Introduction

Autonomous underwater vehicles (AUVs) are unmanned, untethered, self-propelled, and self-controlled robots. These vehicles are capable of operating independently for extended—yet limited—periods of time without the need for continuous human supervision, while efficiently collecting data from a wide variety of sensors, making them highly valuable for scientific, commercial, and military applications. Due to their untethered operation, however, AUVs are inherently constrained by the capacity of their onboard batteries and data storage systems. Consequently, periodic recovery operations are necessary to facilitate the recharging of power sources and the transfer of stored data. Traditionally, these launch and recovery (L&R) procedures have required human intervention when latching and lifting AUVs from the sea surface. Surface L&R operations, particularly in adverse weather conditions and rough seas, pose substantial risks to personnel and equipment.

Autonomous subsurface docking of AUVs could significantly enhance the robustness of L&R operations by allowing execution of a crucial phase of the operation at depths minimally affected by surface waves and wind. This capability would eliminate the need to conduct L&R operations in adverse environmental conditions, thereby extending the operational range of AUVs.

Various approaches to enable subsurface docking have been explored, including the use of protective frames [1–4], flexible wires, rigid poles, and other capture mechanisms [5–7]. Protective frames, while offering enhanced protection, introduce complexity and require precise alignment between the AUV and the docking mechanism. In contrast, flexible wires or rigid poles enable omnidirectional docking, but require the installation of dedicated line-capturing devices on the AUV and the use of precise positioning methods for successful docking.

The localization and docking procedure is typically supported by various sensors, including acoustic sensors, vision cameras, electromagnetic (EM) field sensing, or a fusion of multiple sensors [8]. Acoustic sensors offer long-range detection capabilities but have relatively low resolution and update rates (≈1 Hz) [9]. Vision cameras provide high-precision positioning information but are susceptible to water turbidity and lighting conditions, relying on a continuous line of sight to maintain localization [10,11]. EM guidance, on the other hand, is immune to water conditions and line-of-sight limitations, making it an ideal choice for the critical final stage of docking known as the terminal guidance phase [12–14].

The primary objective of this study was to develop a system (methodology and associated hardware) to provide precise positioning to facilitate terminal docking guidance with a subsurface omnidirectional docking component of a deployable launch and recovery system (LARS), as illustrated in Figure 1. The study aimed to meet the following requirements:

- The system should provide real-time positioning in three dimensions at a minimum rate of 5 Hz.
- The system should not be restricted to specific sectors of the subsurface docking component and must provide a positioning solution for any position and orientation of the AUV and the docking component.
- The system is required to deliver a positioning solution within a range of 1.5 m from the docking component with an accuracy of 5 cm.
- The hardware supporting the developed method should be suitable for installation inside the LARS docking component.
- The system onboard the AUV and the one installed on the docking component should operate as independent asynchronous systems.
- The system should provide a positioning solution in scenarios occurring beyond the line of sight of the AUV's forward-looking camera to enable docking at the AUV's center of gravity point.
- The system's hardware should preferably employ the AUV's onboard sensors and avoid the necessity for the installation of additional external sensors.

To meet the stated requirements and based on its ability to provide precise positioning, particularly in situations where global positioning systems are inaccessible [15–20] or when a direct line of sight to the tracked object cannot be guaranteed [21,22] an EM-based positioning method was selected.

Leveraging our previous work, presented in [23], this paper introduces a novel positioning system for omnidirectional docking guidance. The system utilizes a cost-effective magnetometer placed onboard the AUV and a compact EM beacon integrated into the docking component. Customized signal extraction and positioning algorithms were developed to extract the beacon's signals and determine the AUV's position. Integration of visual markers on the docking component and a camera onboard the AUV were used for a unique initialization process, effectively resolving inherent computational ambiguities related to the magnetic field.

The primary contribution of this work lies in its unique ability to provide a real-time three-dimensional positioning solution without constraining the AUV's operation to a specific sector of the beacon and without requiring continuous synchronization between the transmitting and receiving components.

The system development followed a systematic methodology to ensure a thorough development process, including modeling, algorithm implementation, simulation, laboratory testing, and finally, real-world experimentation. Initially, physical models of both the EM beacon and receiving magnetometers were created to establish the relationships between the beacon's emitted magnetic field and the magnetometer's measured field. Subsequently, signal extraction and positioning algorithms were developed and implemented based on these models. To validate and refine the algorithms further, a beacon simulation was developed and also employed for the adjustment of the beacon properties to meet the system requirements. Subsequently, a functional beacon prototype was constructed and tested in a controlled laboratory environment. Ultimately, the system was integrated into the AUV and LARS and tested in a seawater pool.

Throughout this study, our ALICE AUV [24], a modified configuration of a SPARUS II AUV [25], was used. The proposed approach, however, is adaptable for implementation in various other AUVs.

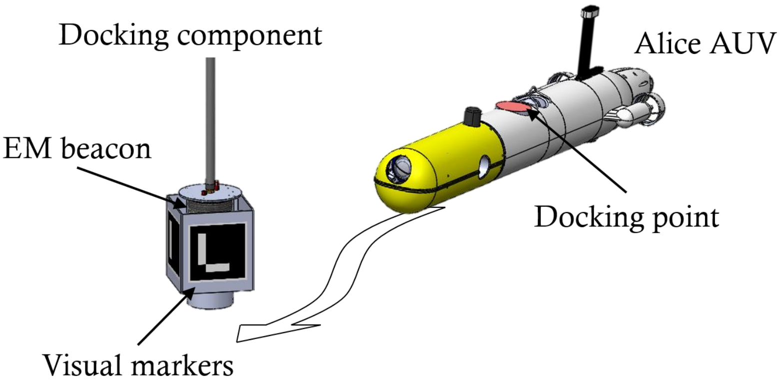

Figure 1. ALICE AUV and the docking component of our LARS system.

2. Related Works

EM-based positioning and guidance systems typically function by detecting an artificial magnetic field generated by dedicated electromagnetic beacons strategically located within the operational area. In this section, we review published works on EM-based positioning and navigation developed for various applications and general purposes that may be adapted to meet the requirements of this study. Thereafter, we review methods specifically designed for underwater docking, examining their compatibility and limitations vis-à-vis the requirements of this study.

Sheinker et al. [16] developed a 3D EM-based localization method using three magnetic beacons and a tri-axial search coil magnetometer. These beacons emitted modulated signals at specific frequencies. A set of lock-in amplifiers (LIAs) was employed to extract these signals from the magnetometer's sampled magnetic flux field. The study evaluated three different beacon placement configurations through simulations and field tests, achieving a localization error below 0.77 m, with a mean error of 0.25 m, in controlled field experiments covering an area of 10 m × 11 m. This method, however, requires the distribution of three beacons in different locations and thus is not applicable for the LARS' docking component.

Andria et al. [21] developed a 3D EM tracking system for surgical navigation comprising five coils that generated AC magnetic fields at distinct frequencies and a 6-DoF magnetic probe. Position estimation was achieved through interpolation and fitting of the measured field to calibration points. This approach yielded a maximum mean error of 3.7 mm within 1 m from the beacon. Similarly, Hu et al. [22] introduced an EM guidance system designed to position medical instruments during spinal surgeries. Their system employed tri-axial transmitting coils and tri-axial receiving coils that were excited by an AC at distinct frequencies. A function fitting and optimization approach calculated the 3D position of the beacon with an accuracy of 1–2 mm and an orientation accuracy below 1° within 0.5 m of the beacon. It is noteworthy, however, that the system's operational range was limited and the complete beacon state determination necessitated prior information. Moreover, these methods can provide complete three-dimensional positioning only when operating within a specified sector of the beacon; otherwise, the positioning solution is not unique. This condition cannot be satisfied when approaching an omnidirectional docking component.

In the field of EM-based AUV docking guidance systems, prior studies have focused primarily on the development of two-dimensional guidance systems designed for directional docking with seabed-fixed stations. Feezor et al. [17] presented an EM-based guidance system for directing an AUV into a cone-shaped docking station. The system utilized three transmitting coils placed on the dock and tri-axial receiving coils installed onboard the AUV. Two of the coils were utilized to generate a signal distinguishing the entrance from the rear side of the dock, while the third coil determined the relative bearing between the AUV and the dock's center line. Successful docking within a range of 25–30 m was achieved. Peng et al. [18] introduced a system featuring a transmitting coil located on the docking station and tri-axial search coils integrated into the AUV. This system was designed specifically for compact and cost-effective AUVs. Utilizing a dedicated signal processing module, the system extracted the amplitude and phase of the transmitting coil, enabling the computation of the bearing between the AUV and the dock entrance, with a detection range of 20 m; however, it is essential to note that these methods only provide relative bearing information and lack range data. As a result, their capability to facilitate accurate docking guidance in three dimensions is limited.

Vandavasi et al. [19] introduced a guidance system utilizing a single transmitting coil positioned on a funnel-shaped dock and two magnetometers installed on a small AUV. The determination of the relative bearing between the AUV and the dock entrance relied on analyzing the difference between the two magnetometer measurements. Estimating the range to the dock involved fitting the measured magnetic field to a spatial magnetic map of the transmitting coil, previously computed using the finite element analysis (FEA) method. Successful demonstrations were achieved within an effective range of 7 m. This method, however, provides only two-dimensional information of bearing and range, and requires the use of two magnetometers and prior development of the magnetic field map. Consequently, it cannot be used for three-dimensional guidance. Lin et al. [20] employed a single transmitting coil and tri-axial receiving coils to guide an AUV into a funnel-shaped dock. The measured amplitudes and phases were used to calculate both the bearing and the range to the dock. To address intensity ambiguity, the guidance was confined to the horizontal plane within an angular range of approximately 10° relative to the dock's center line. Successful docking scenarios were achieved with an accuracy of less than 0.2 m and an orientation within 2.5° in the 6 m range. Nevertheless, this method limits the AUV to operate in a specific sector, and, therefore, it does not meet the requirements for omnidirectional docking.

It is clear that current methods lack the ability to provide comprehensive three-dimensional positioning without imposing restrictions related to a specific area of the beacon or necessitating a precise distribution of multiple beacons. Moreover, to the best of our knowledge, there is no validated existing method specifically tailored for EM-based positioning designed for omnidirectional docking guidance. This underscores the essential need for a method for this type of application in particular.

The subsequent sections of this paper are organized as follows. In Section 3, a detailed overview of the physical structure and mathematical background of the proposed EM-based positioning and guidance system is provided. Section 4 outlines the signal extraction and processing techniques. The algorithm for computing the beacon's position is detailed in Section 5. Section 6 describes the implementation of the signal extraction and positioning algorithms. The validation of the proposed positioning method through simulation is discussed in Section 7. The system's implementation and corresponding laboratory experiments are presented in Section 8. Section 9 details the integration of the system within the LARS and in our AUV, ALICE. It also outlines the configuration and presents the results of experiments conducted in real scenarios within our seawater pool. Finally, Section 10 summarizes the primary findings and presents concluding remarks.

3. Physical Model and Mathematical Formulation

3.1. EM Beacon

The EM beacon used in this study consists of three transmitting coils, denoted $i = 1,2,3$ and positioned in an orthogonal configuration, as shown in Figure 2. To differentiate the beacon's artificial field from other magnetic fields, each coil is driven by a sinusoidal signal with a distinct frequency. The physical arrangement of the system's current configuration, where the beacon is installed inside the docking component and the magnetometer is installed within the AUV, allows us to assume that the sensing magnetometer operates at distances greater than the beacon's diameter but shorter than the signals' wavelength. As a result, each coil can effectively be modeled as a magnetic dipole. Furthermore, given the system's requirement for close-range operation and its submersion to a depth where surface effects are negligible, it is reasonable to assume that the medium is homogeneous seawater with constant permeability.

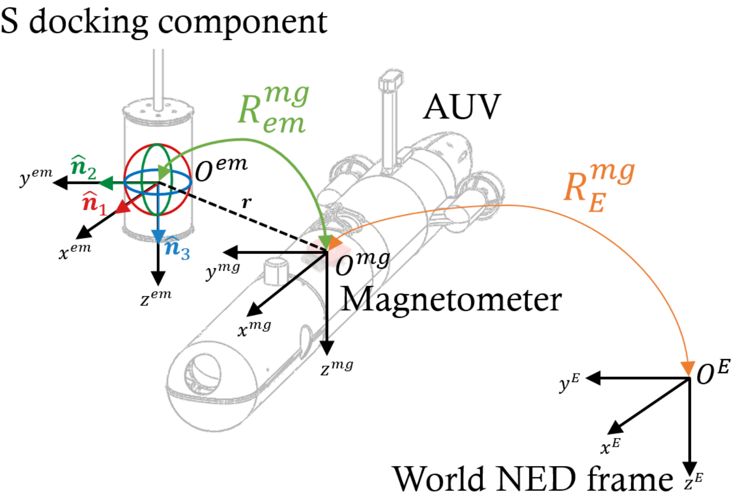

Figure 2. EM beacon, magnetometer, and world NED (North, East, Down) coordinate frames. For the purpose of this study, we assume that the onboard tri-axial magnetometer frame coincides with the AUV frame.

In this work, the main coordinate frames are the EM beacon frame $\{O^{em}, x^{em}, y^{em}, z^{em}\}$, with its origin fixed to the center of the beacon, and the axes aligned with the coils' axes, the magnetometer frame $\{O^{mg}, x^{mg}, y^{mg}, z^{mg}\}$, and the world NED (North, East, Down) frame $\{O^E, X^E, Y^E, Z^E\}$. For the purpose of this study, it was assumed that the magnetometer's frame coincides with the AUV's frame. The vector $\mathbf{r} = [x^{em}, y^{em}, z^{em}]^T$ represents the spatial position of O^{mg} relative to the origin O^{em}. Consequently, the magnetic flux density of the i'th coil, $\mathbf{B}_i^{em} = [B_{ix}^{em}, B_{iy}^{em}, B_{iz}^{em}]^T$, can be expressed by [26]:

$$\mathbf{B}_i^{em}(\mathbf{r}) = \frac{\mu}{4\pi}\left[\frac{3(\mathbf{M}_i \cdot \mathbf{r})\mathbf{r} - \mathbf{M}_i|\mathbf{r}|^2}{|\mathbf{r}|^5}\right] \tag{1}$$

where $\mu = \mu_0 \cdot \mu_r$ is the permeability of the medium, with $\mu_0 = 4 \cdot \pi \cdot 10^{-7} [\mathrm{kg} \cdot \mathrm{m} \cdot \mathrm{s}^{-2} \cdot \mathrm{A}^{-2}]$ the permeability of the free space, and μ_r the relative permeability of the medium (approximately 1 for seawater). The magnetic moments of the three transmitting coils, denoted by $\mathbf{M}_i$, are defined as follows:

$$\mathbf{M}_i = A_i \cdot N_i \cdot I_i \cdot \sin(\omega_i t + \phi_i) \cdot \hat{\mathbf{n}}_i \tag{2}$$

where A_i represents the coil's cross-sectional area, N_i denotes the number of turns, I_i is the current, ω_i is the frequency, and ϕ_i is the phase of the coils' excitation current. The orientation of each coil in the EM beacon frame is defined by $\hat{\mathbf{n}}_i$, where:

$$\hat{\mathbf{n}}_1 = [1, 0, 0]^T, \quad \hat{\mathbf{n}}_2 = [0, 1, 0]^T, \quad \hat{\mathbf{n}}_3 = [0, 0, 1]^T. \tag{3}$$

The rotation between the NED and AUV frames is defined by $\mathbf{R}_E^{mg}$, and the rotation between the AUV and the EM beacon frames is defined by $\mathbf{R}_{em}^{mg}$, where $\mathbf{R} = \mathbf{R}_\psi \mathbf{R}_\vartheta \mathbf{R}_\varphi$, obtained by multiplication of the rotations $\mathbf{R}_\psi$, $\mathbf{R}_\vartheta$, and $\mathbf{R}_\varphi$ about the x-, y-, and z-axes, respectively, with:

$$\mathbf{R}_\varphi = \begin{pmatrix} 1 & 0 & 0 \\ 0 & \cos\varphi & -\sin\varphi \\ 0 & \sin\varphi & \cos\varphi \end{pmatrix}, \quad \mathbf{R}_\vartheta = \begin{pmatrix} \cos\vartheta & 0 & \sin\vartheta \\ 0 & 1 & 0 \\ -\sin\vartheta & 0 & \cos\vartheta \end{pmatrix}, \quad \mathbf{R}_\psi = \begin{pmatrix} \cos\psi & -\sin\psi & 0 \\ \sin\psi & \cos\psi & 0 \\ 0 & 0 & 1 \end{pmatrix}. \tag{4}$$

The rotationbetween the NED and the AUV frames is defined by the angles ψ_E^{mg}, ϑ_E^{mg}, and φ_E^{mg}, and the rotation between the AUV and the beacon frames is defined by the angles ψ_{em}^{mg}, ϑ_{em}^{mg}, and φ_{em}^{mg}. The coordinate frames and the beacon notation are illustrated in Figure 2.

3.2. Receiving Magnetometers

The magnetometer, located onboard the AUV, measures the magnetic flux density along three orthogonal directions x^{mg}, y^{mg}, and z^{mg}. The acquired signals encompass contributions from diverse sources, including the EM beacon signals, Earth's geomagnetic field, and ambient noise. Assuming that errors arising from sensor cross-axis misalignment, nonlinearity, and scale factor can be disregarded, the measured magnetic flux density, denoted as $\mathbf{B}^{mg}$, is provided by the following expression:

$$\mathbf{B}^{mg} = \mathbf{R}_{em}^{mg}\mathbf{B}^{em} + \mathbf{R}_E^{mg}\mathbf{B}^E + noise \tag{5}$$

where $\mathbf{B}^{em} = \sum_{i=1}^{3} \mathbf{B}_i^{em}$ and $\mathbf{B}_i^{em}$, defined by Equation (1). The geomagnetic field, referenced to the world NED frame, is denoted by $\mathbf{B}^E = [B_x^E, B_y^E, B_z^E]^T$.

4. Signal Processing

The magnetic flux density of the i'th coil, $\mathbf{B}_i^{mg}$, was extracted from the magnetometer's measurements using a digital implementation of lock-in amplifiers (LIAs) [27]. These LIAs detect both the amplitudes and phases of signals that correlate with internally generated reference signals, as defined by:

$$s_i = 2 \cdot \sin(\omega_i t) \tag{6}$$
$$s_i^{\frac{\pi}{2}} = 2 \cdot \cos(\omega_i t)$$

where ω_i is the frequency of each coil and $s_i^{\frac{\pi}{2}}$ is a signal shifted by a phase of $\frac{\pi}{2}$ with respect to s_i. To identify the beacon's signals, the sampled signals, $\mathbf{B}^{mg}$, were multiplied by s_i and $s_i^{\frac{\pi}{2}}$.

Denoting the combination of the geomagnetic field, other beacon signals, and noise by $n(t)$ and the components of $\mathbf{B}^{mg} = [B_x^{mg}, B_y^{mg}, B_z^{mg}]^T$ by $j = x, y, z$, the result of this multiplication of each component of $\mathbf{B}^{mg}$ with the reference signals is expressed as follows:

$$B_j^{mg} \cdot s_i = 2 \cdot |B_{ij}^{mg}| \cdot \sin(\omega_i t + \phi_{ij}) \cdot \sin(\omega_i t) + n(t) \cdot \sin(\omega_i t) \tag{7}$$

$$B_j^{mg} \cdot s_i^{\frac{\pi}{2}} = 2 \cdot |B_{ij}^{mg}| \cdot \sin(\omega_i t + \phi_{ij}) \cdot \cos(\omega_i t) + n(t) \cdot \cos(\omega_i t). \tag{8}$$

Equations (7) and (8) can be rewritten as:

$$B_j^{mg} \cdot s_i = |B_{ij}^{mg}| \cdot \left[\cos(\phi_i) - \cos(2\omega_i t + \phi_{ij})\right] + n(t) \cdot \sin(\omega_i t) \tag{9}$$

$$B_j^{mg} \cdot s_i^{\frac{\pi}{2}} = |B_{ij}^{mg}| \cdot \left[\sin(2\omega_i t + \phi_{ij}) + \sin(\phi_{ij})\right] + n(t) \cdot \cos(\omega_i t). \tag{10}$$

Applying low-pass filters to Equations (9) and (10) removes their time-dependent components while retaining their DC values:

$$\left[B_j^{mg} \cdot s_i\right]_{LPF} = |B_{ij}^{mg}| \cdot \cos(\phi_{ij}) \tag{11}$$

$$\left[B_j^{mg} \cdot s_i^{\frac{\pi}{2}}\right]_{LPF} = |B_{ij}^{mg}| \cdot \sin(\phi_{ij}). \tag{12}$$

Finally, the magnitudes and phases of the beacon's signals are obtained by:

$$|B_{ij}^{mg}| = \sqrt{(|B_{ij}^{mg}| \cdot \cos(\phi_{ij}))^2 + (|B_{ij}^{mg}| \cdot \sin(\phi_{ij}))^2} \tag{13}$$

and

$$\phi_{ij} = \tan^{-1}\left(\frac{|B_{ij}^{mg}| \cdot \sin(\phi_{ij})}{|B_{ij}^{mg}| \cdot \cos(\phi_{ij})}\right). \tag{14}$$

A schematic description of the LIA components precisely adjusted for signal extraction at the frequency ω_i is presented in Figure 3.

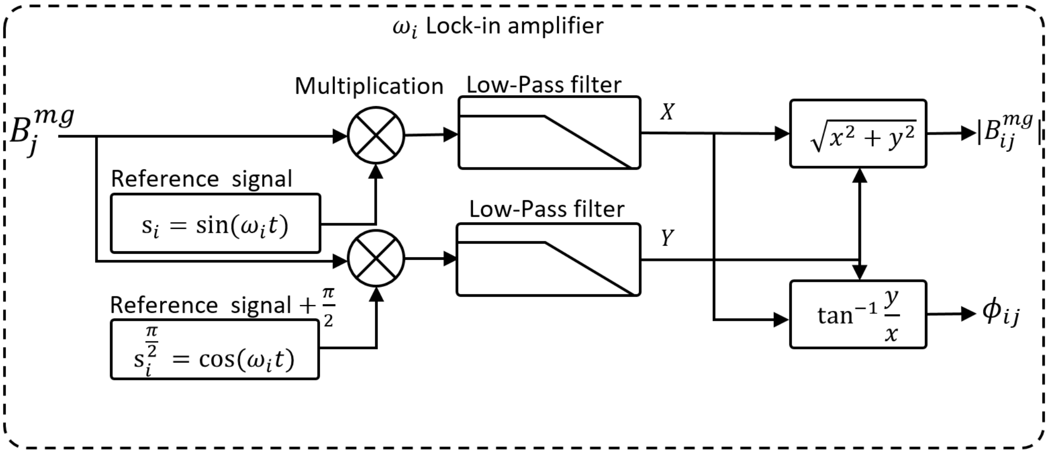

Figure 3. A schematic description of a lock-in amplifier for the extraction of a signal at the frequency ω_i.

5. Computing the Beacon Location

5.1. Determination of the Beacon Direction

To determine the position vector, **r**, and the rotation angles of $\mathbf{R}_{em}^{mg}$, the magnitudes calculated in Equation (13) are incorporated into Equation (1):

$$\mathbf{R}_{em}^{mg\,T}\mathbf{B}_i^{mg} = \frac{\mu}{4\pi}\left[\frac{3(\mathbf{M}_i \cdot \mathbf{r})\mathbf{r} - \mathbf{M}_i|\mathbf{r}|^2}{|\mathbf{r}|^5}\right]. \tag{15}$$

The EMfield produced by the beacon, however, showed multiple locations where the magnitudes of the magnetic flux density were equivalent in various regions, as illustrated in Figure 4. Consequently, determining a unique position was only possible after resolving the signs of $|B_{ij}^{mg}|$. This challenge was overcome by analyzing the phases ϕ_{ij} computed by Equation (14) and using the property that, corresponding to the direction of the magnetic field, the phases exhibit variations when intersecting the axes of the coil, as demonstrated in Figure 5a,b.

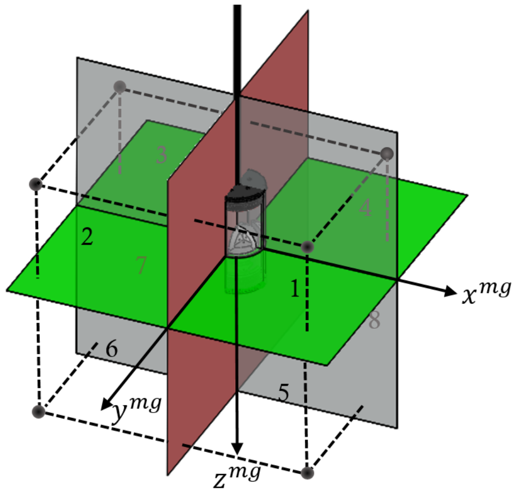

Figure 4. Eight beacon sectors highlighting points with identical magnetic field values.

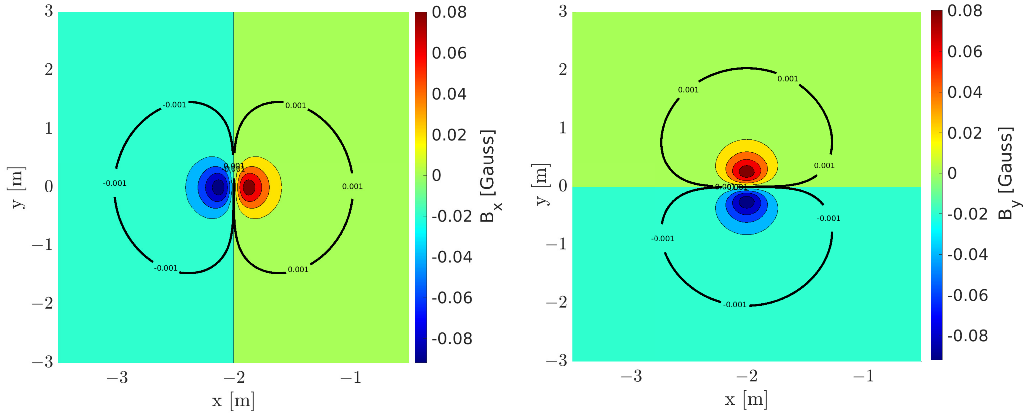

(a) (b)

Figure 5. (**a**) The magnetic flux density of B_x^{em} and (**b**) B_y^{em} on the plane $z = 0.5m$ was calculated by solving Equation (1) for a coil with a diameter of 0.12 m, 370 turns, and a DC current of 3.2 A. Contours at the 0.001 G level illustrate the dipole field's shape, with the $X = 0$ line in (**a**) and $Y = 0$ in (**b**), indicating points where components of the magnetic flux density change direction.

Since the EM beacon and reference signals operate in separate frames, an initial calibration process was employed to establish the spatial relationship between position coordinates and measured phases. This calibration occurred during a"handshake" between the vision and EM guidance phases, when both the AUV magnetometer and the forward-looking camera simultaneously detected the docking component, as depicted in Figure 6. In this process, the relative position, $\mathbf{r}_0$, and the rotation of the AUV with respect to the beacon $\mathbf{R}_{hs}^{mg}$ were determined by the visual marker pose estimation algorithm, and a "handshake" frame was established. This frame, fixed to the origin of the AUV $\{O^{hs}\} = \{O^{mg}\}$ and aligned with the beacon's frame during the "handshake" moment, facilitates the decomposition of the rotation of the beacon with respect to the AUV, $\mathbf{R}_{em}^{mg}$, into the rotation of the beacon with respect to the "handshake" frame, denoted as $\mathbf{R}_{em}^{hs}$, and the rotation of the AUV with respect to the "handshake" frame, denoted as $\mathbf{R}_{hs}^{mg}$, and computed with the following angles:

$$\begin{aligned} \psi_{hs}^{mg} &= \psi_0 + \Delta\psi_{EKF} \\ \vartheta_{hs}^{mg} &= \vartheta_0 + \Delta\vartheta_{EKF} \\ \varphi_{hs}^{mg} &= \varphi_0 + \Delta\varphi_{EKF} \end{aligned} \tag{16}$$

where ψ_0, ϑ_0, and φ_0 represent the rotational angles between the beacon and the AUV, as measured by the visual marker detection algorithm at the moment of the "handshake", and $\Delta\psi_{EKF}$, $\Delta\vartheta_{EKF}$, and $\Delta\varphi_{EKF}$ denote the changes in the AUV's orientation between the measurement moment and the "handshake" moment, as estimated by the AUV's navigation filter. Consequently, the "handshake" frame enables the measurement of magnetic flux densities and phase variations independently of the AUV's orientation.

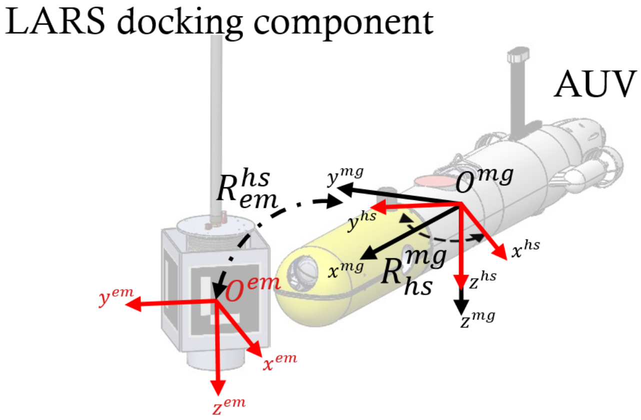

Figure 6. Spatial configuration of the AUV, docking component, beacon, body, and reference frames at the "handshake" moment.

It is essential to understand that phase computation is highly susceptible to interference. Therefore, achieving accurate positioning, which demands reliable signals from at least six field components, may not always be feasible. This challenge is particularly pronounced when the AUV is positioned near one of the beacon's axes or at a distance where signal weakening becomes noticeable.

To enhance the robustness of position computation, an alternative approach was developed. This involved determining the relative direction to the beacon using either two components of one signal or three components of distinct signals. This was accomplished by assigning a unique combination of in-phase and anti-phase components to each beacon sector. As illustrated in Table 1, however, each combination of phases corresponds to two potential solutions. For instance, Sectors 1 and 7 share identical phase combinations, introducing ambiguity in identifying the correct solution. To address this ambiguity, transitions that are physically implausible or constrained by the dynamics of the AUV and the docking component were excluded. For example, direct transitions between Sectors 1 and 7 were ruled out as they would intersect with the docking component. Similarly, transitions between diagonal Sectors 1 and 6 are considered implausible, given that the AUV performs decoupled vertical and horizontal movements during the terminal guidance phase.

Table 1. Relations between the signal phase and position, where "+" and "-" denote the in-phase and anti-phase field components, respectively.

Sector	Direction	ϕ_{x1}, ϕ_{y1}	ϕ_{y2}, ϕ_{z2}	ϕ_{x3}, ϕ_{z3}
1	x > 0, y > 0, z > 0	+, +	+, +	+, +
7	x < 0, y < 0, z < 0	+, +	+, +	+, +
2	x > 0, y < 0, z > 0	+, -	-, +	-, -
8	x < 0, y > 0, z < 0	+, -	-, +	-, -
3	x < 0, y < 0, z > 0	-, -	+, -	+, -
5	x > 0, y > 0, z < 0	-, -	+, -	+, -
4	x < 0, y > 0, z > 0	-, +	-, -	-, +
6	x > 0, y < 0, z < 0	-, +	-, -	-, +

5.2. Computation of the Beacon Position

The position of the AUV with respect to the beacon, represented by the six variables of $\mathbf{r}$ and $\mathbf{R}_{em}^{mg}$, was determined by solving the system of Equation (15). This system consists of nine equations, with $\mathbf{B}_1^{mg}$, $\mathbf{B}_2^{mg}$, $\mathbf{B}_3^{mg}$. Consequently, the equations in (15) form an overdetermined system. To address this, an optimization technique, specifically the Levenberg–Marquardt (LM) method [28], was employed to find values for $\mathbf{r}$ and $\mathbf{R}_{em}^{hs}$ that minimize $\mathbf{f}_i$, as defined by:

$$\mathbf{f}_i(\mathbf{r}, \mathbf{R}_{em}^{hs}) = \frac{\mu}{4\pi}\left[\frac{3(\mathbf{M}_i \cdot \mathbf{r})\mathbf{r} - \mathbf{M}_i|\mathbf{r}|^2}{|\mathbf{r}|^5}\right] - \mathbf{R}_{em}^{hs\,T}\,\mathbf{R}_{hs}^{mg\,T} \cdot |\mathbf{B}_i^{mg}| \cdot sign\{\mathbf{B}_i^{mg}\}. \tag{17}$$

6. Algorithm Implementation

The developed signal extraction and positioning algorithms were implemented as ROS nodes [29]. Figure 7 provides a schematic representation of the algorithms, illustrating the data processing flow, which includes the acquisition of an ArUco visual marker [30] and the beacon's magnetic field, computation of the "handshake" frame, the extraction of signals by the LIAs, and subsequent processes for direction detection and position computation. To elaborate, an attitude and heading reference system (AHRS), equipped with tri-axial magnetometers, gyros, and accelerometers, along with an embedded extended Kalman filter (EKF) algorithm, was utilized to obtain measurements of $\mathbf{B}^{mg}$ (calibrated to hard and soft iron magnetic disturbances) and the angles ψ_{EKF}, ϑ_{EKF}, and φ_{EKF}, estimated by the EKF.

To mitigate the impact of the AUV motion on the measured signals and reduce the influence of high-frequency noise, $\mathbf{B}^{mg}$ was filtered by a fourth-order Butterworth band-pass filter with a central frequency of 20 Hz and a bandwidth of 10 Hz. This filter was implemented using a C++ library for real-time digital implementation of IIR filters [31].

Following filtration, the signals were multiplied by the rotation matrix, $\mathbf{R}_{hs}^{mg}$, to compensate for the AUV's rotation and transform $\mathbf{B}^{mg}$ into the "handshake" frame. The rotational matrix. $\mathbf{R}_{hs}^{mg}$. was computed by implementing Equation (4) and the angles described by Equation (16), where ψ_0, ϑ_0, and φ_0 were determined using the ArUco marker detection algorithm [32]. The algorithm uses acquired images of markers with unique binary patterns and prior knowledge of their type and size to calculate their position and orientation. The markers were aligned with the beacon axes to provide the beacon's angles with respect to the AUV.

Subsequently, the transformed signals, $\mathbf{R}_{hs}^{mg}\mathbf{B}^{mg}$, were processed by a digital implementation of LIAs. This process involved multiplying the signals by time-dependent sine and cosine functions corresponding to the beacon's frequencies. These products were then filtered using fourth-order Butterworth low-pass filters with a cutoff frequency of 0.4 Hz. The filters were digitally implemented using the IIR filter library. The filter outputs were further processed to extract the amplitudes $|\mathbf{B}_1^{mg}|$, $|\mathbf{B}_2^{mg}|$, and $|\mathbf{B}_3^{mg}|$ and the phases $\boldsymbol{\phi}_1$, $\boldsymbol{\phi}_2$, and $\boldsymbol{\phi}_3$ by implementing Equations (13) and (14).

Following this, the obtained amplitudes and phases, along with the initial position $\mathbf{r}_0 = [x_0, y_0, z_0]$, were inserted into a dedicated direction detection function to determine the signs of $|\mathbf{B}_1^{mg}|$, $|\mathbf{B}_2^{mg}|$, and $|\mathbf{B}_3^{mg}|$ by computing the relative direction to the beacon. The function utilized the initial position, $\mathbf{r}_0$, to set the signs of $|\mathbf{B}_1^{mg}|$, $|\mathbf{B}_2^{mg}|$, and $|\mathbf{B}_3^{mg}|$ using specialized zero-crossing detection logic. This logic meant switching the signs based on the measured phases by identifying instances where the phases shifted by 180°, as schematically described by Algorithm 2. To mitigate erroneous crossings caused by frequency discrepancies between the beacon and reference signals [33] or noise, the phases were continuously assessed using a moving window comprising 200 measurements. Within this window, the periodic average of the signal, the standard deviation, and the rate of change of the phases were calculated. Empirically determined threshold values were applied to identify and exclude erroneous crossings.

To detect the relative position based only on phase information, a simplified version of Table 1, containing only four possible states of phase combinations (shown in Table 2), was utilized. The latter simplified table serves as a look-up table in conjunction with the motion-constraint logic discussed in Section 5. The specific procedure is elaborated in Algorithm 1.

Ultimately, the signed values of $\mathbf{B}_1^{mg}$, $\mathbf{B}_2^{mg}$, and $\mathbf{B}_3^{mg}$ were inserted into the position computation function. This function employed the LM (least squares) method, implemented using the Mobile Robot Programming Toolkit (MRPT) library [34], to compute $\mathbf{r}$ and $\mathbf{R}_{em}^{hs}$ by solving Equation (17), as outlined in Algorithm 2.

To enhance the robustness of the computation, the solver was constrained to provide a solution within the maximum detection range of 2.5 m around the beacon. This constraint was implemented through the introduction of a "penalty" function:

$$f_4(\mathbf{r}) = \begin{cases} 1 & \text{if } |\mathbf{r}| > 2.5 \text{ m} \\ 0 & \text{else} \end{cases}. \tag{18}$$

Furthermore, the number of computed variables was reduced by setting the values of the computed pitch and roll of the docking component to zero. This decision was based on the assumption that the docking component, fixed to the surface platform via a flexible wire, primarily induces heave motion due to surface waves, with significant pitch and roll motions not expected. Consequently, the angles ϑ_{em}^{hs} and φ_{em}^{hs} were constrained to zero, reducing the number of independent variables and strengthening the robustness of the calculation. To prevent positioning errors resulting from weak signals, position computation was activated only when at least one value of $\mathbf{B}_{ij}^{mg}$ exceeded a threshold of 0.03 G.

Algorithm 1: Direction computation algorithm

```
Data: $\mathbf{r}_0, \mathbf{R}_{hs}^{mg}, \boldsymbol{\phi}_1, \boldsymbol{\phi}_2, \boldsymbol{\phi}_3$
Result: sector
if ArUco marker detected then
    sector ← $\mathbf{r}_0$;
    $\boldsymbol{\Phi} \leftarrow \boldsymbol{\phi}_1, \boldsymbol{\phi}_2, \boldsymbol{\phi}_3$;
    Sector_initialized = True
if Sector_initialized then
    prev_sector = sector;
    state = Look-up Table 2 ($\boldsymbol{\Phi}$);
    if state = 1 and prev_sector = 1 or 2 or 4 or 5 then
        sector = 1
    else if state = 1 and prev_sector = 7 or 6 or 8 or 3 then
        sector = 7
    else if state = 2 and prev_sector = 2 or 1 or 3 or 6 then
        sector = 2
    else if state = 2 and prev_sector = 8 or 5 or 7 or 4 then
        sector = 8
    else if state = 3 and prev_sector = 3 or 2 or 4 or 7 then
        sector = 3
    else if state = 5 and prev_sector = 5 or 6 or 8 or 1 then
        sector = 5
    else if state = 4 and prev_sector = 4 or 1 or 3 or 8 then
        sector = 4
    else if state = 6 and prev_sector = 6 or 5 or 7 or 2 then
        sector = 6
```

To refine the solution accuracy further, a refinement process was implemented. Via this, the outliers that exceed the maximum expected positional variation based on the AUV's maximum speed during the terminal guidance maneuvers (0.15 m/s) are detected and excluded. Additionally, an averaging technique was applied over a moving window that included 50 computed positions.

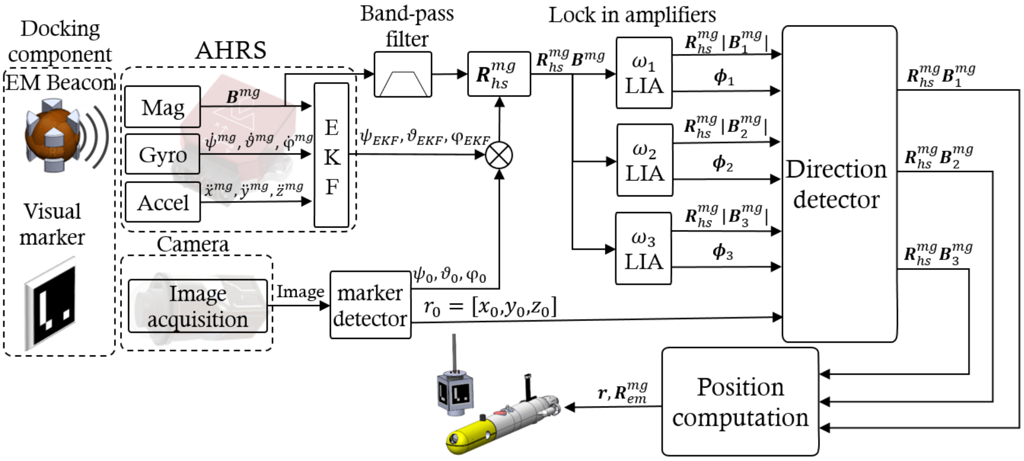

Figure 7. Schematic description of the signal extraction and positioning algorithms, where Mag, Gyro, and Accel denote the AHRS' magnetometer, gyros, and accelerometers.

Table 2. Simplified table with four possible combinations of phases, where "+" and "-"denote the in-phase and anti-phase field components, respectively.

State	Direction	ϕ_{x1}, ϕ_{y1}	ϕ_{y2}, ϕ_{z2}	ϕ_{x3}, ϕ_{z3}
1	x > 0, y > 0, z > 0	+, +	+, +	+, +
2	x > 0, y < 0, z > 0	+, -	-, +	-, -
3	x < 0, y < 0, z > 0	-, -	+, -	+, -
4	x < 0, y > 0, z > 0	-, +	-, -	-, +

Algorithm 2: Position computation algorithm

```
Data: $\mathbf{B}^{em}, \mathbf{R}_{hs}^{mg}, \mathbf{r}_0$
Result: $\mathbf{r}, \mathbf{R}_{em}^{mg}$
$prev\_\boldsymbol{\phi}_{1,2,3} \leftarrow 0$;
if $ArUco\_marker\_detected$ then
    $\mathbf{R}_{hs}^{mg} \leftarrow [\psi_0 + \Delta\psi, \vartheta_0 + \Delta\vartheta, \varphi_0 + \Delta\varphi]$;
    $\mathbf{r}_0 \leftarrow [x_0, y_0, z_0]$;
    for $i \leftarrow 1$ to 3 do
        $sign\{\mathbf{B}_i^{mg}\} = sign\left\{\frac{\mu}{4\pi}\left[\frac{3(\mathbf{M}_i \cdot \mathbf{r}_0)\mathbf{r}_0 - \mathbf{M}_i|\mathbf{r}_0|^2}{|\mathbf{r}_0|^5}\right] \cdot \mathbf{R}_{hs}^{mg}\right\}$;
    $Phase\_initialized$ = True
if $Phase\_initialized$ then
    for $i \leftarrow 1$ to 3 do
        $|\mathbf{B}_i^{mg}|, \boldsymbol{\phi}_i \leftarrow LIA_i\{\mathbf{B}^{mg}\}$ ;
        for $j \leftarrow 1$ to 3 do
            if $\phi_{ij} \cdot prev\_\phi_{ij} < 0$ then
                $sign\{\boldsymbol{B}_{ij}^{mg}\} = -sign\{\boldsymbol{B}_{ij}^{mg}\}$
            $prev\_\phi_{ij} = \phi_{ij}$
    $\boldsymbol{r}, \boldsymbol{R}_{hs}^{mg} \leftarrow \frac{\mu}{4\pi}\left[\frac{3(\boldsymbol{M}_i \cdot \boldsymbol{r})\boldsymbol{r} - \boldsymbol{M}_i|\boldsymbol{r}|^2}{|\boldsymbol{r}|^5}\right] - \mathbf{R}_{hs}^{mg\,T}\mathbf{R}_{em}^{hs\,T} \cdot |\boldsymbol{B}_i^{mg}| \cdot sign\{\boldsymbol{B}_i^{mg}\}$
```

7. Simulation-Based Validation

A dedicated beacon simulation was utilized to assess the performance of the developed algorithms in signal extraction and positioning. This simulation generated a synthetic magnetic flux density using Equation (5), considering specific beacon properties outlined in Table 3, along with parameters such as relative position, $\mathbf{r}$, and orientation, $\mathbf{R}_{em}^{hs}$.

To mimic the magnetometer properties described in Table 4 and accurately simulate real-world measurements, the signals were discretized based on the magnetometer's sampling rate and resolution. White noise with a standard deviation of 2 mG was incorporated, and a geomagnetic field vector of $\boldsymbol{B}_E = [0.2\ \text{G}, 0.13\ \text{G}, 0.35\ \text{G}]$ was defined.

Table 3. Transmitting beacon properties.

Beacon core diameter (⌀)	0.12 m
Wire cross-section diameter (⌀)	0.7 mm
Coil 1 input current (I_1)	1.53 A
Coil 2 input current (I_2)	1.3 A
Coil 3 input current (I_3)	1.4 A
Coil 1 frequency (f_1)	16 Hz
Coil 2 frequency (f_2)	20 Hz
Coil 3 frequency (f_3)	25 Hz
Coil 1 number of turns (N_1)	370 turns
Coil 2 number of turns (N_2)	370 turns
Coil 3 number of turns (N_3)	370 turns

Table 4. Magnetometer properties.

Magnetometer	
Model	Vectornav VN100/VN300
Type	MEMS
Scale	±2.5 G
Noise Density	$140\ \mu\text{G}/\sqrt{\text{Hz}}$
Resolution	1.5 mG
Sampling Frequency	200 Hz

To assess the algorithm's robustness comprehensively against potential errors and sensor misalignment encountered in real-world applications, the simulation was repeated with simulated sensor misalignment errors. These errors included angular deviations of 5° in roll, pitch, and yaw between the magnetometer and the AUV frames, along with a 10% error in modeling magnetic moments, $\boldsymbol{M}_i$.

The algorithms underwent evaluation in two distinct scenarios. The first focused on static positioning, introducing 16 fixed positions evenly spaced at intervals of 10 cm. Positioning accuracy was assessed using the root mean square error (RMSE) value calculated over 600 solutions for each point.

The results of the static positioning simulation, as illustrated in Figure 8, indicated an accuracy of 3 mm with precisely configured beacon parameters, 2.5 cm in the presence of some uncertainty in the beacon parameters, and 5.2 cm when simulating magnetometer misalignment.

In the dynamic scenario, linear motion was simulated at a constant speed of 0.1 m/s along a predefined path. In this scenario, as presented in Figure 9, an accuracy of 13 cm was achieved with accurate knowledge of the beacon parameters, 15 cm in the presence of uncertainties in the beacon parameters, and 14 cm with applied magnetometer misalignment. A summary of the results for static and dynamic simulations is provided in Table 5. These findings confirm the algorithm's ability to compute positions with sufficient accuracy for guiding the AUV to the docking position. It is evident, however, that precision levels are notably affected by onboard magnetometer misalignment and inaccuracies in the beacon’s properties. To enhance position accuracy, these parameters need to be verified and carefully adjusted.

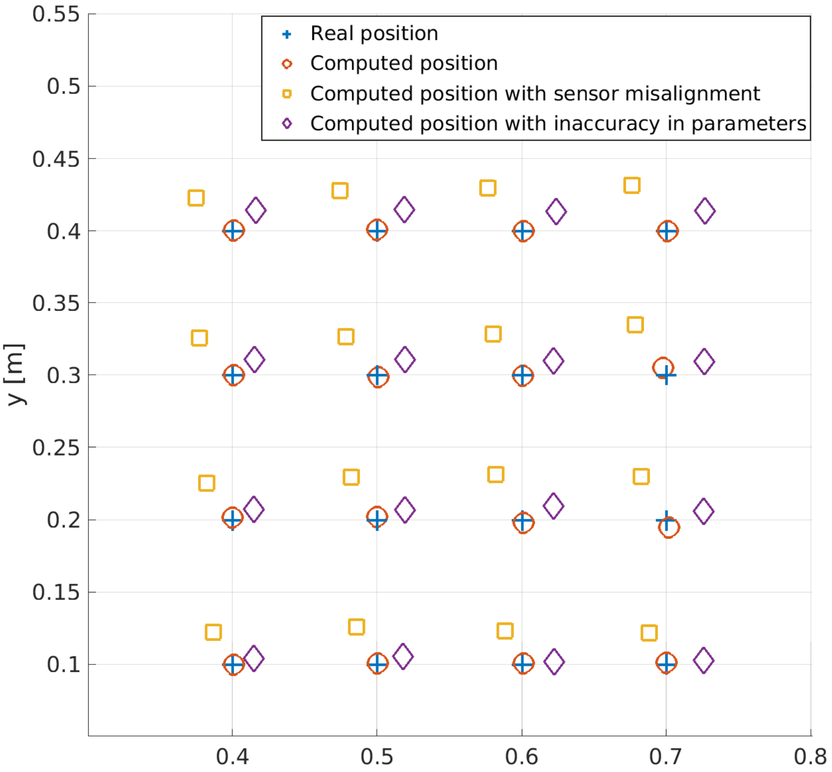

Figure 8. Simulation results for position computation at selected points.

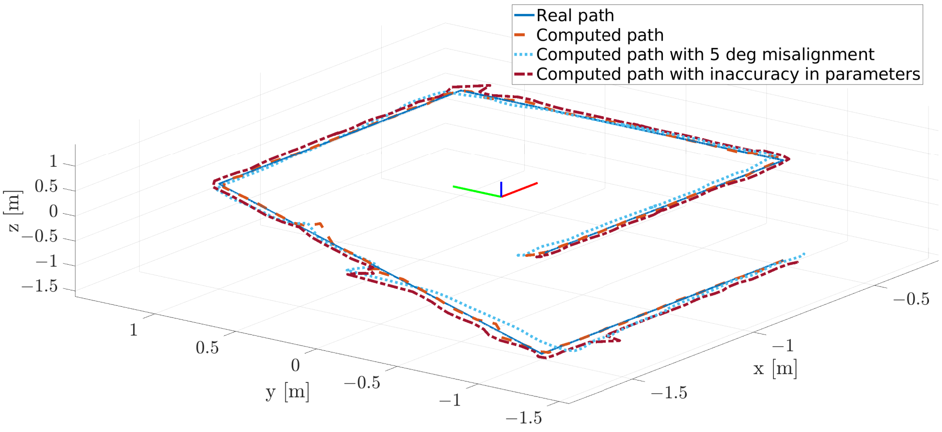

Figure 9. Simulation results for position computation along a path.

Table 5. Summary of the simulation results.

Scenario	RMSE (m)
Static	0.0031
Static with inaccuracy in parameters	0.0252
Static with sensor misalignment	0.052
Dynamic	0.13
Dynamic with inaccuracy in parameters	0.148
Dynamic with sensor misalignment	0.144

8. In-Laboratory Prototype Testing

8.1. Lab System Implementation

A functional prototype of the beacon and the signal generation system was developed for real-world testing, as illustrated in Figure 10. The construction of the beacon involved winding three orthogonal copper coils around a 3D-printed ABS core with a 0.12 m diameter. Each coil comprised approximately 370 turns. The beacon's dimensions were designed to fit into the 6-inch cylindrical housing of the docking component. The coils were powered by three alternating sine signals, generated by an AD9958 multi-channel frequency synthesizer and subsequently amplified using three mono-channel 130 W, 24 VDC CS8683 digital amplifiers. These signals were configured to operate at frequencies of 16 Hz, 20 Hz, and 25 Hz to ensure adequate sampling by the receiving magnetometer.

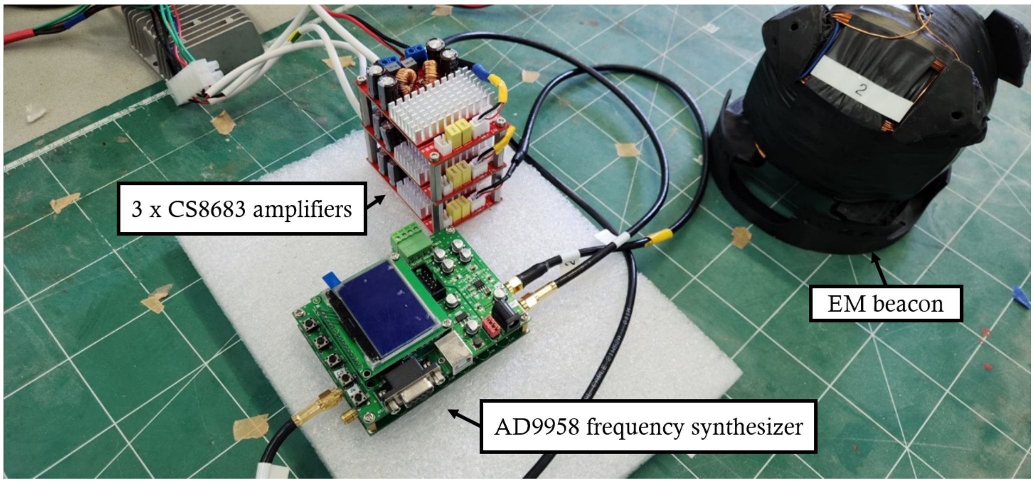

Figure 10. Prototype of the experimental EM beacon and the signal generation system in the lab experiments.

In the laboratory experiments, the magnetic flux density was measured using the tri-axial magnetometer embedded inside the VectorNav VN-300 AHRS. This system was linked to a PC for measurement sampling and executing the signal extraction and positioning algorithms outlined in Section 6. For comprehensive specifications for both the beacon and the magnetometer, see Tables 3 and 4, respectively.

To achieve precise calibration of the input signals, the amplified signals were initially measured using an oscilloscope. The measurements indicated frequency errors of 0.6%, as summarized in Table 6. Even though these errors were minimal, they might have introduced significant measurement errors and affected the stability of the output signal [33]. To mitigate these issues, fine-tuning of the reference signals was conducted by adjusting their frequencies until the output of the phase exhibited stable and consistent values. Figure 11 illustrates this process, demonstrating phase computation inconsistency during static measurement, with a minor error of 0.3% in the reference signal frequency. The figure also illustrates the successful fine-tuning of the signal achieved at a frequency of 15.95 Hz.

Table 6. Summary of the frequency errors, as measured by the oscilloscope.

Preset Frequency	Measured Frequency (% Max Error)
16 Hz	15.91–15.96 Hz (0.56%)
20 Hz	19.86–19.95 Hz (0.7%)
25 Hz	24.85–24.98 Hz (0.6%)

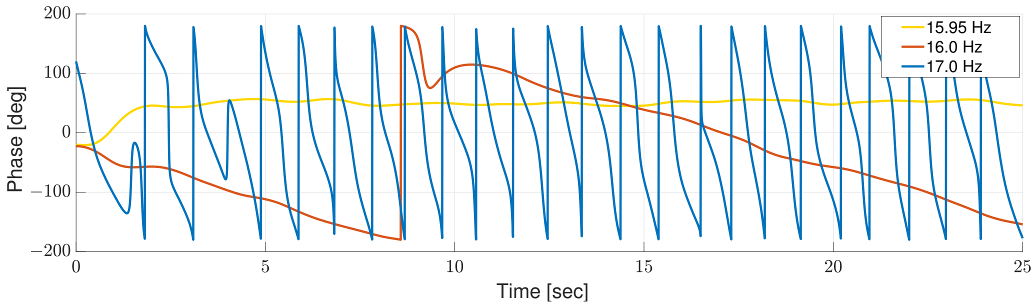

Figure 11. Phase computation from a single field component as computed for three different frequencies of reference signals.

In addition, cross-talk voltages [15] resulting from interactions between the beacon coils were measured and their impact was assessed. To measure cross-talk voltage, a signal was supplied to one coil while simultaneously measuring the induced voltage on the other coils. The recorded cross-talk voltages consistently stayed below 30 mV during the test, confirming their negligible influence on the overall beacon signal.

8.2. Lab System Experiments

The system's positioning accuracy was assessed in a controlled laboratory experiment. In this setup, the beacon was placed on a flat plane with grid intervals of 5 cm. Much like the static simulation scenario, the magnetometer was positioned at 16 discrete points in close proximity to the beacon, enabling a direct comparison between the algorithm's results and the known positions. This experimental configuration is illustrated in Figure 12.

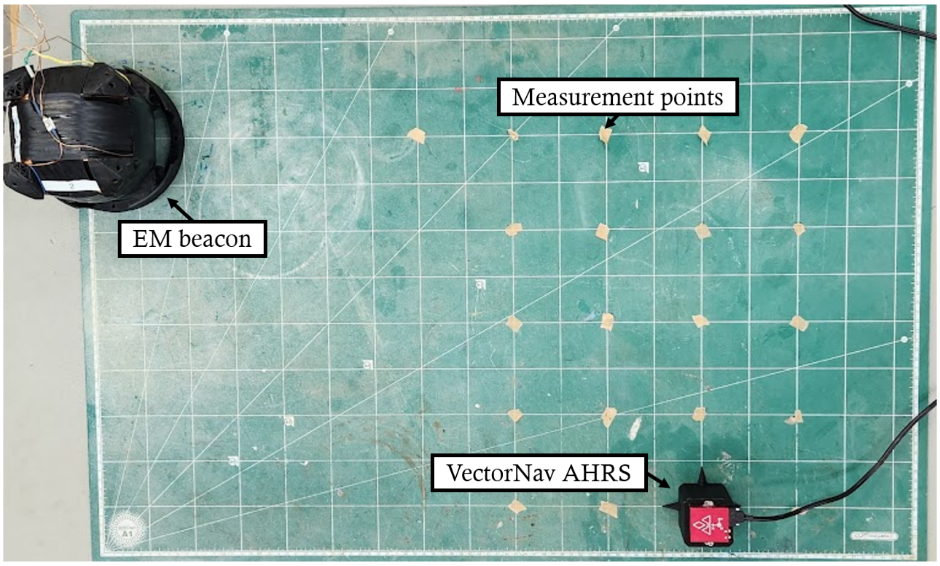

Figure 12. Setup of the lab experiment.

To initialize the algorithm, the position data from the first measurement point were used. The precision of the computed positions was carefully evaluated by measuring the error between the average value of 45 positioning solutions and the actual position of each point. To account for installation errors, each point was adjusted by an overall offset vector, $\mathbf{X}_{offset}$ = [0.102 m, 0.058 m, 0.003 m]. This offset was based on the average error between the computed and actual points, calculated by:

$$\mathbf{X}_{offset} = \frac{1}{16}\sum_{i=1}^{16}(\mathbf{X}_i^p - \langle \mathbf{X}_i^c \rangle). \tag{19}$$

Here, $\mathbf{X}_i^p$ represents the actual position and $\langle \mathbf{X}_i^c \rangle$ denotes the average position derived from 45 solutions for each point. This adjustment procedure aimed to mitigate errors related to the installation of the beacon. Additionally, an assessment was conducted by measuring the relative distance between every pair of adjacent points, leveraging the inherent precision of the measuring grid.

The experimental outcomes, depicted in Figure 13, along with the positioning errors illustrated in Figures 14 and 15, highlight the system's real-time ability to calculate the position relative to the beacon, achieving an average accuracy of under 3 cm. Inaccuracies stemming from variations in the coils' properties and the installation process can significantly affect positioning precision. Hence, a systematic calibration procedure is essential before operational usage to rectify such discrepancies.

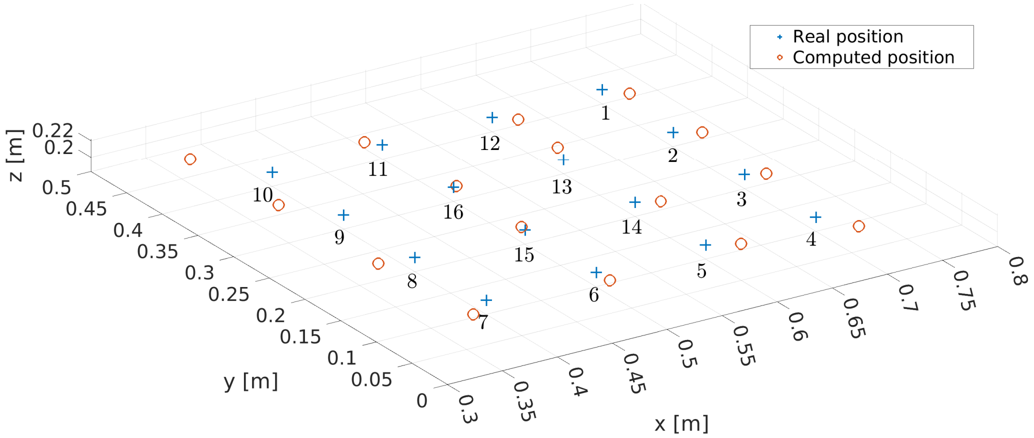

Figure 13. Positioning results for 16 measurement points in the lab experiment.

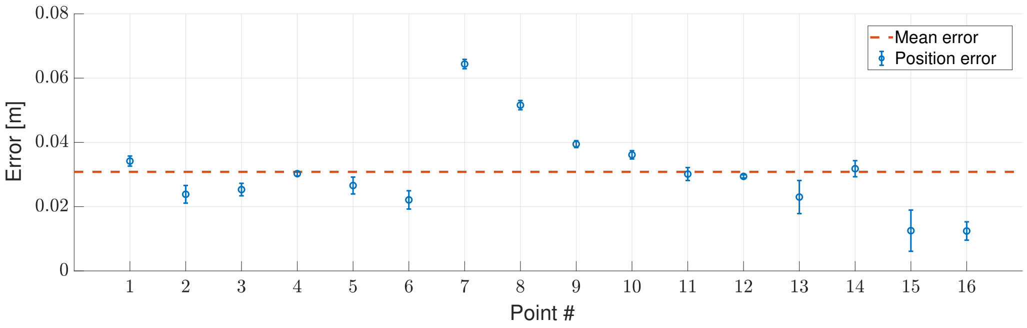

Figure 14. Positioning errors with respect to the measurement points in the lab experiment.

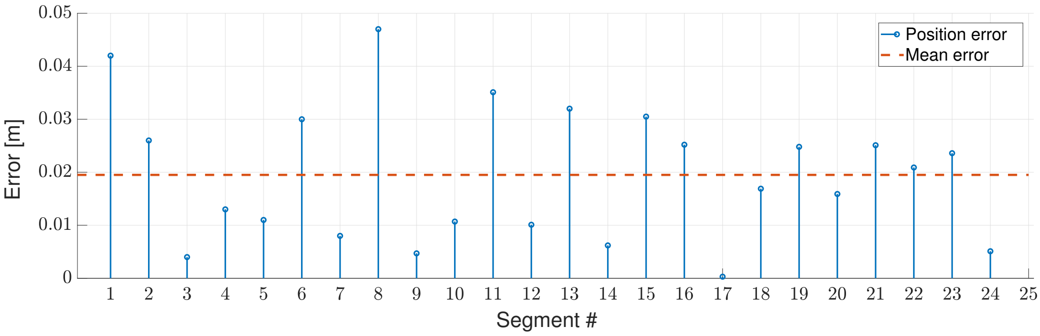

Figure 15. Relative distance errors with respect to the measurement grid segments in the lab experiment.

9. System Integration and Experimental Validation

Following the successful outcomes of the laboratory experiments, the developed system was integrated into the LARS. The signal generator and amplifiers were installed within an electronic enclosure located on the LARS floating platform, as depicted in Figure 16. A remote power-enable switching circuit was implemented to enable remote activation of the beacon when the platform was deployed. The amplified signals were transferred to the beacon via a slip ring mechanism, enabling the deployment of the docking component to depths of up to 10 m.

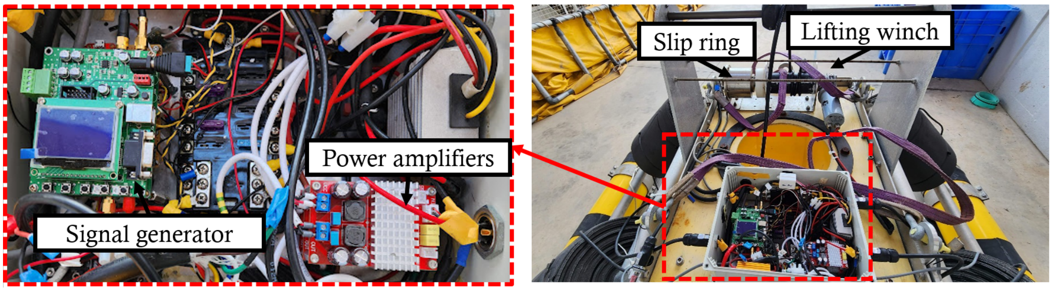

Figure 16. The signal generator and the power amplifiers inside the electronics box of the LARS system.

The beacon was integrated into the docking component. For heat management, the beacon housing was filled with 3M NOVEC™ 7100 engineered fluid, which allowed improved heat dissipation from the beacon. Four ArUco markers were positioned around the housing to facilitate the visual guidance phase and the "handshake" process. These markers were arranged in a configuration that enabled the beacon's position and orientation to be captured, irrespective of the approach direction, thereby permitting omnidirectional docking. The installation of the beacon inside the housing and the positioning of the visual markers are illustrated in Figure 17.

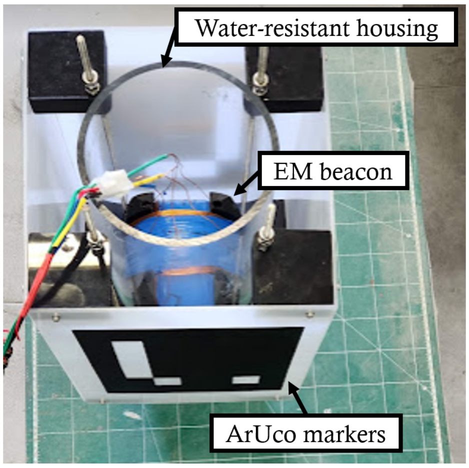

Figure 17. A prototype of the experimental EM beacon and signal generation system, as used in the lab experiment.

Initially, for the AUV's sensor setup, the AUV's native magnetometer, integrated with the ADIS16488A AHRS, was used; however, its relatively modest sampling rate of 123 Hz was found to be inadequate. Accordingly, the VectorNav VN-100 AHRS, equipped with a magnetometer similar to the VN-300, was integrated to provide a higher sampling rate of 200 Hz. The AUV's onboard camera (Allied Vision Prosilica GT6600) was employed to detect the visual markers. To ensure precise position and orientation data, the camera's water-resistant housing incorporated a dome port to minimize refractions that could lead to image distortions. In addition, the camera's intrinsic parameters were calibrated using a calibration board in our facility's seawater pool.

To latch the AUV, a lifting electromagnet was installed beneath the housing of the docking component and a metal attachment plate was fixed on top of the AUV's hull near its center of gravity, as shown in Figure 18.

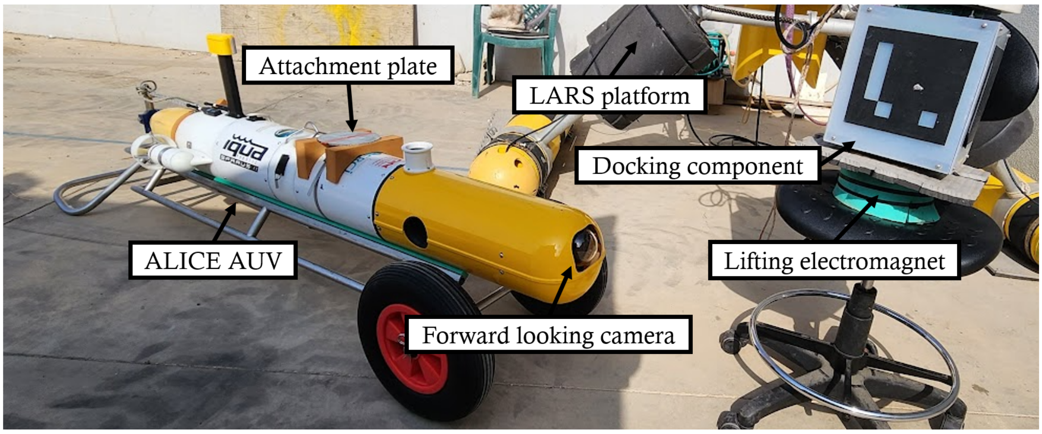

Figure 18. The attachment plate located on ALICE and the lifting electromagnet embedded in the bottom of the docking component.

9.1. Assessment of the Integrated System's Accuracy and Detection Range

Before conducting docking experiments in the pool, the integrated system underwent assessment in an experiment focused on determining the prototype's detection distance and accuracy. To test the system's detection range, the Vectornav VN300 INS was placed at 13 equidistant points, spaced at 0.1 m intervals up to 1.5 m, as shown in Figure 19. The positioning results, depicted in Figure 20 with the error analyses presented in Figure 21, demonstrated that the system successfully detected the beacon at distances up to 1.5 m with sufficient accuracies of less than 4 cm up to a range of 0.9 m and 8 cm up to a range of 1.5 m. Notably, the average errors and standard deviations increased beyond a distance of 1 m. For the specific task of docking, the highest precision is required as the AUV approaches very close to the docking component. The system achieved the necessary level of accuracy.

9.2. Docking Maneuvering Sequence

The maneuvering sequence during the visual and EM guidance phases utilized ALICE's capability for decoupled motion control in heave, sway, surge, and yaw [24]. The docking sequence in the terminal guidance was implemented by a state machine, utilizing the SMACH state machine library for building hierarchical state machines [35]. The sequence, outlined in Figure 22, is activated when the ArUco marker detection algorithm detects one of the markers installed on the docking component. Following detection, the beacon position is obtained and used to control the AUV as it moves to the "handshake" position, located at a distance of 1.4 m between the AUV's center of gravity and the beacon, with the AUV's heading facing the marker. This specific distance was chosen to position the onboard magnetometer as close as possible to the beacon while ensuring continued visual detection of the markers. The EM positioning algorithm is triggered upon approaching the "handshake" position. During this process, the values of $\mathbf{r}_0$ and $\mathbf{R}_{hs}^{mg}$ are input into the algorithm to calibrate the phases and determine the beacon's initial direction. Additionally, magnetometer measurements are excluded from the AUV's navigation filter to prevent drift in the heading computation. This exclusion becomes necessary when in close proximity to the docking component, as the measurements of the geomagnetic field are significantly disturbed by the magnetic fields of the beacon and the EM lifting device.

After initialization, the AUV is directed to descend below the docking component by adding 0.5 m to the beacon's computed position. This measure is implemented to prevent potential collisions between the docking component and the AUV's hull and appendages. Upon reaching this depth, the AUV's horizontal controller is activated to position the AUV horizontally beneath the docking component, maintaining a margin of 15 cm. The position computed by the EM positioning algorithm serves as the desired goal point. Within this range, the slow ascent process is initiated by turning off the vertical thruster, allowing the positive buoyancy of the AUV to gradually lift until it is securely attached to the lifting electromagnet. Throughout the terminal guidance, the AUV's surge and sway motion controllers are restricted to a maximum speed of 0.1 m/s. Moreover, it should be noted that the AUV's navigation filter provides a dead-reckoning positioning solution to facilitate continued control in scenarios where the magnetometers lose signals from the beacon.

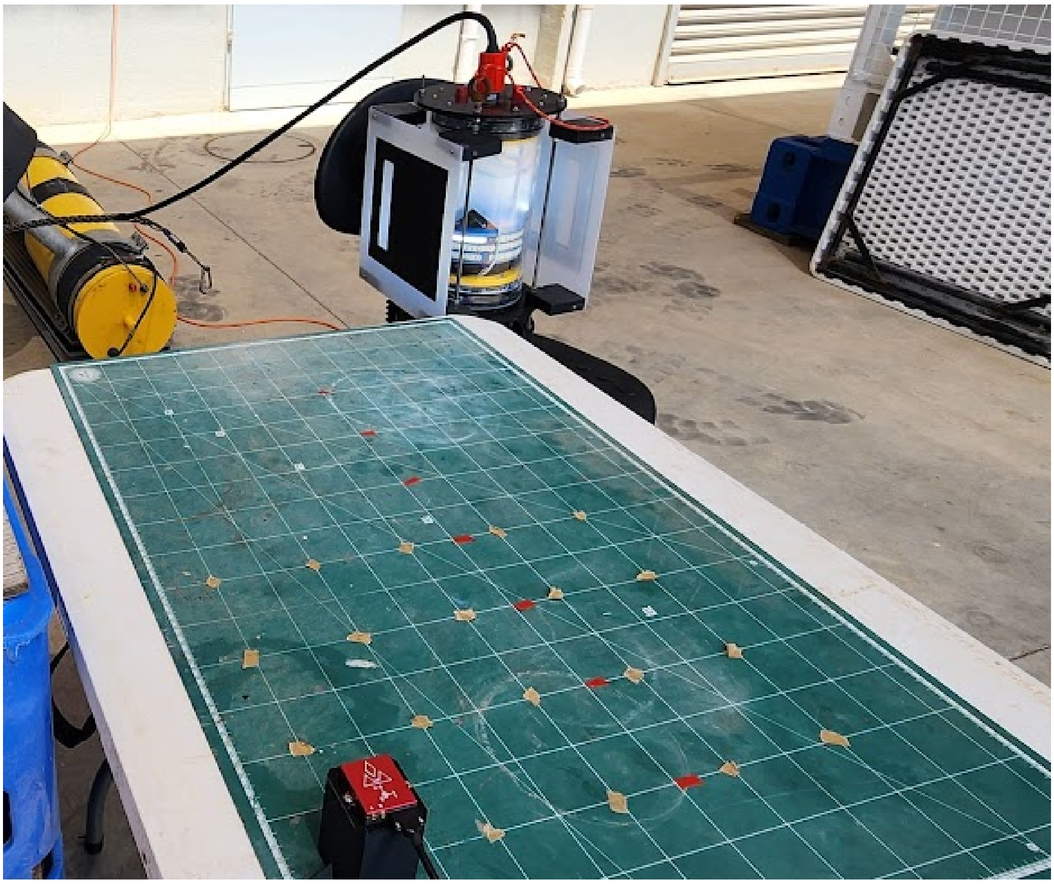

Figure 19. The LARS docking component, with the EM beacon and the ArUco markers, during one experiment.

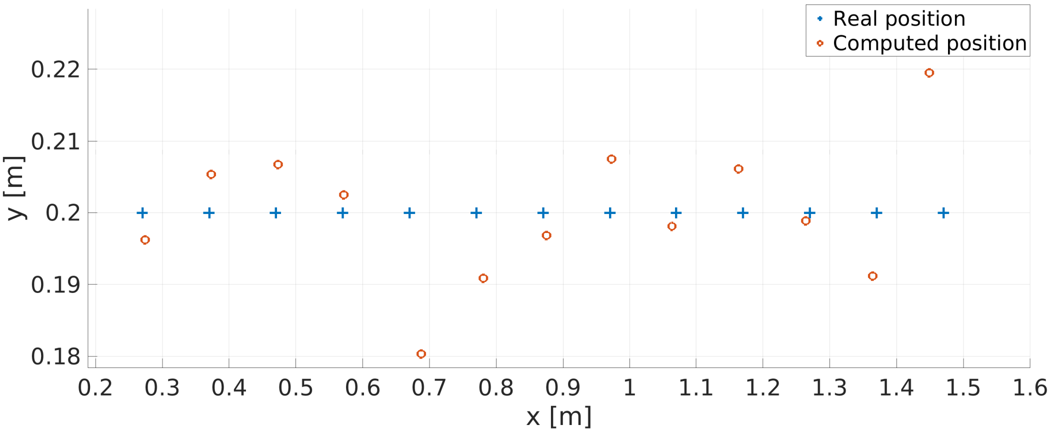

Figure 20. Positioning results of the integrated system in a controlled experiment.

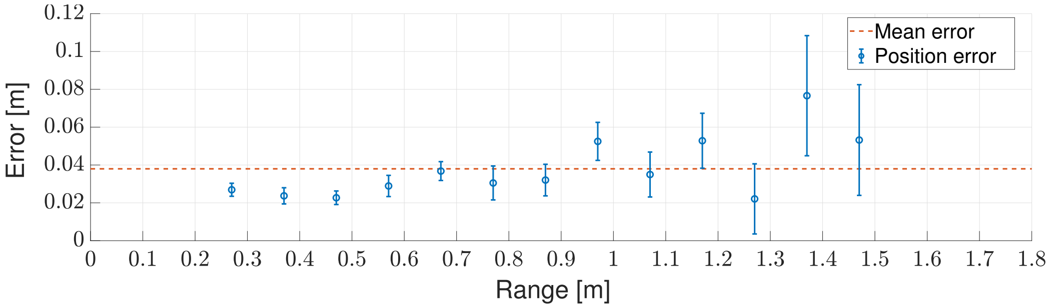

Figure 21. Error evaluation for the integrated system in a controlled experiment.

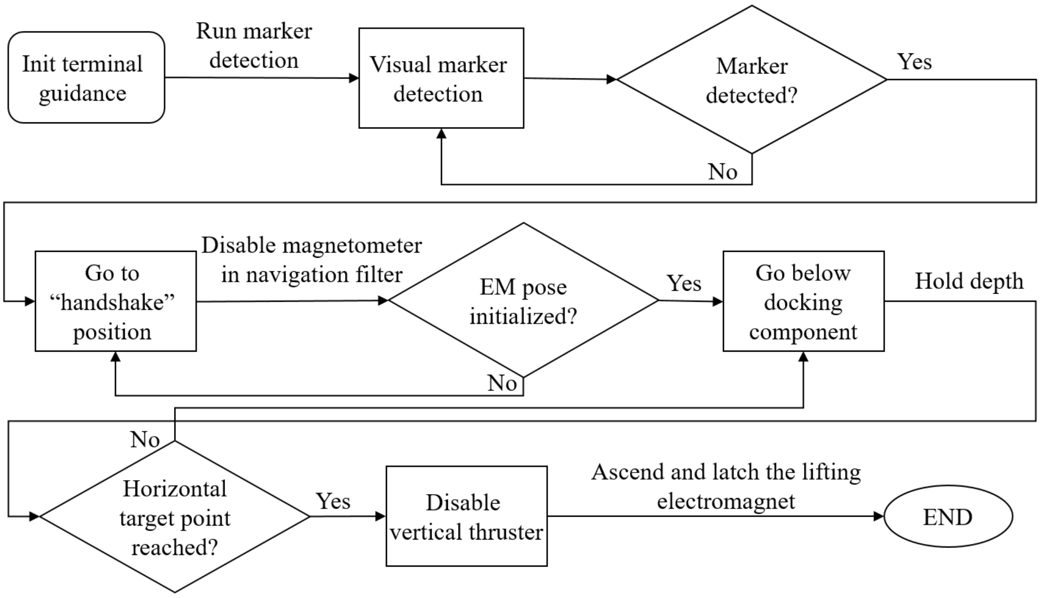

Figure 22. Schematic description of the terminal guidance phase.

9.3. Pool Trials of the Terminal Docking Phase

Ultimately, the system's ability to provide guidance during the terminal phase of docking was assessed in a real pool environment. The test occurred in our 9 m × 3 m × 2.8 m (L × W × H) seawater pool, involving both the entire configuration of the ALICE AUV and the docking component.

In this experiment, the docking component was submerged to a depth of approximately 1.5 m below the surface, with the AUV positioned at a distance where the specified marker detection algorithm could detect the ArUco markers. At this point, the docking sequence commenced, and the AUV autonomously approached the "handshake" position using the markers, as depicted in Figure 23. When the AUV reached a distance of 1.4 m from the beacon, the position of the beacon, determined from the markers, was used to initiate the EM guidance. After initialization, the AUV descended to a depth of 0.5 m below the docking component, as depicted in Figure 24. At this point, the AUV maintained a consistent depth and regulated its lateral and forward movements based on the EM positioning algorithm until reaching the predetermined tolerance of 15 cm below the component.

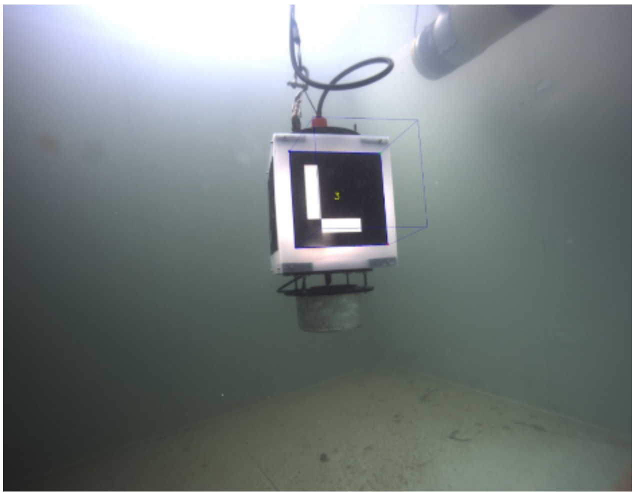

Figure 23. The docking component in the pool experiment, as identified by ALICE's onboard camera and the ArUco marker detection algorithm.

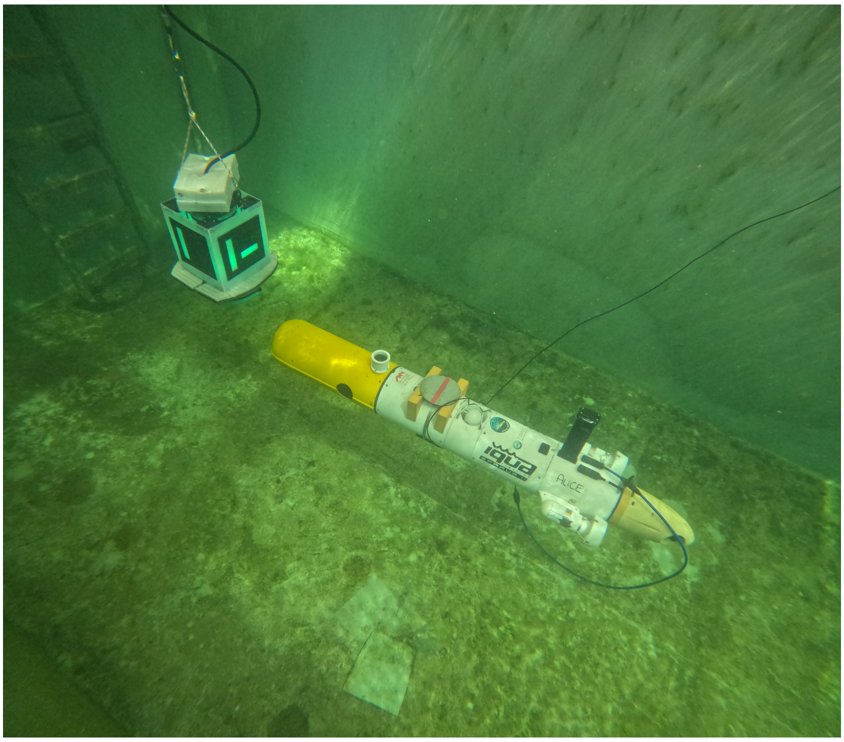

Figure 24. The setup of the pool experiment, consisting of the omnidirectional docking component and the ALICE AUV.

10. Conclusions

In this research, a novel EM guidance method was introduced to facilitate precise three-dimensional navigation of an AUV toward a LARS docking component. Notably, this method does not necessitate continuous line-of-sight between the LARS component and the AUV.

A significant contribution of this method, in comparison to others, lies in its ability to offer accurate positioning without restricting the AUV's maneuverability to a specific sector of the docking component, allowing for an omnidirectional approach to the docking component. To enable comprehensive 3D positioning, an innovative initialization process aided by a vision-based positioning algorithm was incorporated. The system's development and the algorithm's performance were rigorously evaluated using dedicated simulations. Following this, a functional prototype of the system was developed, and a series of experiments were conducted to assess the system's accuracy and effectiveness in guiding our ALICE AUV during the terminal docking phase. The experimental results demonstrated high accuracy, deviating less than 4 cm within a range of 0.7 m and 8 cm within a range of 1.5 m. These results highlight the method's ability to guide the AUV effectively during the docking process. In the final phase of the study, the EM beacon system was integrated into our LARS, and the algorithmic framework was implemented in the ALICE AUV control system to guide it through an actual docking task in a controlled pool environment. The experiments conducted in this controlled setting validated the system's ability to provide precise positioning guidance during the critical terminal docking phase. They also highlighted some additional improvements that may enhance the method's robustness. Possible improvements are:

- Designing the beacon such that it can generate stronger magnetic fields. This improvement has the potential to enhance both the detection range and the efficiency of the signal extraction algorithm, leading to improved determination of signal phases.
- Enabling the AUV to utilize a magnetometer with increased sensitivity and a higher sampling rate. This approach would allow the AUV to detect weak magnetic fields and enable the beacon to generate magnetic fields at higher frequencies. The objective is to enhance the system's capability to filter these signals out from other magnetic fields effectively.

In addition to implementing the suggested improvements for this method, future research will involve conducting additional experiments in different scenarios, both in controlled environments and at sea. It should be noted that a significant benefit of the proposed method is its potential extension to meet positioning needs for diverse applications that align with its specifications. Furthermore, there is potential for the development of advanced AI-based methods to enhance computational efficiency and accuracy in signal extraction and position computation.

Author Contributions: The contribution of each author is specified as follows: conceptualization, Y.G. and M.G.; methodology, Y.G. and M.G.; software, Y.G.; validation, Y.G.; writing—original draft preparation, Y.G. and M.G.; writing—review and editing, M.G.; visualization, Y.G.; supervision, M.G. All authors have read and agreed to the published version of the manuscript.

Funding: This research was funded by the Leona M. and Harry B. Helmsley Charitable Trust and The Maurice Hatter Foundation.

Data Availability Statement: Datasets and code available on request from the authors.

Acknowledgments: The authors would like to thank Nir Zagdanski, Uri Katz, Amir Dayan, and Uri Graiver.

Conflicts of Interest: The authors declare no conflicts of interest.

List of Symbols

$\hat{\mathbf{n}}_i$	Orientation of coil *i* with respect to the beacon frame
μ	Permeability of the medium
μ_0	Permeability of the free space
μ_r	Relative permeability of the medium
ω_i	Signal frequency of coil *i*
ϕ_i	Signal phase of coil *i*
$\mathbf{B}^{em}$	Complete magnetic flux density of the EM beacon
$\mathbf{B}_i^{em}$	Magnetic flux density of coil *i*

$\mathbf{B}^{E}$	Geomagnetic flux density
$\mathbf{B}^{mg}$	Measured magnetic flux density
$\mathbf{B}_i^{mg}$	Measured magnetic flux density of coil i
$\mathbf{M}_i$	Magnetic moment of coil i
$\mathbf{r}$	Position of the origin O^{mg} relative to the origin O^{em}
$\mathbf{r}_0$	Position of the origin O^{mg} relative to the origin O^{em} at the moment of the "handshake"
$\mathbf{R}_{em}^{hs}$	Rotation matrix between the EM beacon and "handshake" frames
$\mathbf{R}_{em}^{mg}$	Rotation matrix between the EM beacon and AUV frames
$\mathbf{R}_{E}^{mg}$	Rotation matrix between the NED and AUV frames
$\mathbf{R}_{hs}^{mg}$	Rotation matrix between the "handshake" and AUV frames
$\{\ddot{x}^{mg}, \ddot{y}^{mg}, \ddot{z}^{mg}\}$	AUV's linear accelerations, as measured by the AHRS' accelerometers
$\{\dot{\varphi}^{mg}, \dot{\vartheta}^{mg}, \dot{\psi}^{mg}\}$	AUV's angular velocities, as measured by the AHRS' gyros
$\{\varphi_E^{mg}, \vartheta_E^{mg}, \psi_E^{mg}\}$	Rotation angles between the NED and the AUV frames
$\{\varphi_0, \vartheta_0, \psi_0\}$	Rotation angles between the EM beacon and the AUV frames at the moment of the "handshake"
$\{\varphi_{EKF}, \vartheta_{EKF}, \psi_{EKF}\}$	AUV's rotation angles, as estimated by the EKF
$\{\varphi_{em}^{hs}, \vartheta_{em}^{hs}, \psi_{em}^{hs}\}$	Rotation angles between the EM beacon and "handshake" frames
$\{\varphi_{em}^{mg}, \vartheta_{em}^{mg}, \psi_{em}^{mg}\}$	Rotation angles between the EM beacon and the AUV frames
$\{\varphi_{hs}^{mg}, \vartheta_{hs}^{mg}, \psi_{hs}^{mg}\}$	Rotation angles between the "handshake" and the AUV frames
A_i	Cross-sectional area of coil i
I_i	Current of coil i
N_i	Number of turns of coil i
$s_i^{\frac{\pi}{2}}$	Reference signal with a frequency i and a phase of $\frac{\pi}{2}$
s_i	Reference signal with a frequency i
$\{O^{em}, x^{em}, y^{em}, z^{em}\}$	EM beacon frame
$\{O^{E}, x^{E}, y^{E}, z^{E}\}$	World NED frame
$\{O^{hs}, x^{hs}, y^{hs}, z^{hs}\}$	"Handshake" frame
$\{O^{mg}, x^{mg}, y^{mg}, z^{mg}\}$	AUV and magnetometer frame

References

1. Gu, H.t.; Meng, L.; Bai, G.; Zhang, H.; Lin, Y.; Liu, S. Automated recovery of the UUV based on the towed system by the USV. In Proceedings of the 2018 OCEANS-MTS/IEEE Kobe Techno-Oceans (OTO), Kobe, Japan, 28–31 May 2018; pp. 1–7.
2. Sarda, E.I.; Dhanak, M.R. A USV-based automated launch and recovery system for AUVs. *IEEE J. Ocean. Eng.* **2016**, *42*, 37–55. [CrossRef]
3. Jalving, B.; Faugstadmo, J.E.; Vestgard, K.; Hegrenaes, O.; Engelhardtsen, O.; Hyland, B. Payload sensors, navigation and risk reduction for AUV under ice surveys. In Proceedings of the OCEANS 2008, Woods Hole, MA, USA, 13–14 October 2008; pp. 1–8.
4. Lin, M.; Lin, R.; Yang, C.; Li, D.; Zhang, Z.; Zhao, Y.; Ding, W. Docking to an underwater suspended charging station: Systematic design and experimental tests. *Ocean Eng.* **2022**, *249*, 110766. [CrossRef]
5. Kimball, P.W.; Clark, E.B.; Scully, M.; Richmond, K.; Flesher, C.; Lindzey, L.E.; Harman, J.; Huffstutler, K.; Lawrence, J.; Lelievre, S.; et al. The ARTEMIS under-ice AUV docking system. *J. Field Robot.* **2018**, *35*, 299–308. [CrossRef]
6. Sarda, E.I.; Dhanak, M.R. Launch and recovery of an autonomous underwater vehicle from a station-keeping unmanned surface vehicle. *IEEE J. Ocean. Eng.* **2018**, *44*, 290–299. [CrossRef]
7. Piskura, J.C.; Purcell, M.; Stokey, R.; Austin, T.; Tebo, D.; Christensen, R.; Jaffre, F. Development of a robust Line Capture, Line Recovery (LCLR) technology for autonomous docking of AUVs. In Proceedings of the OCEANS 2016 MTS/IEEE Monterey, Monterey, CA, USA, 19–23 September 2016; pp. 1–5.
8. Hildebrandt, M.; Christensen, L.; Kirchner, F. Combining cameras, magnetometers and machine-learning into a close-range localization system for docking and homing. In Proceedings of the OCEANS 2017-Anchorage, Anchorage, AK, USA, 18–21 September 2017; pp. 1–6.
9. Miranda, M.; Beaujean, P.P.; An, E.; Dhanak, M. Homing an unmanned underwater vehicle equipped with a DUSBL to an unmanned surface platform: A feasibility study. In Proceedings of the 2013 OCEANS-San Diego, San Diego, CA, USA, 23–27 September 2013; pp. 1–10.
10. Maki, T.; Shiroku, R.; Sato, Y.; Matsuda, T.; Sakamaki, T.; Ura, T. Docking method for hovering type AUVs by acoustic and visual positioning. In Proceedings of the 2013 IEEE International Underwater Technology Symposium (UT), Tokyo, Japan, 5–8 March 2013; pp. 1–6.
11. Fan, S.; Liu, C.; Li, B.; Xu, Y.; Xu, W. AUV docking based on USBL navigation and vision guidance. *J. Mar. Sci. Technol.* **2019**, *24*, 673–685. [CrossRef]

12. Kusche, R.; Schmidt, S.O.; Hellbrück, H. Indoor Positioning via Artificial Magnetic Fields. *IEEE Trans. Instrum. Meas.* **2021**, *70*, 1–9. [CrossRef]
13. Dai, H.; Song, S.; Zeng, X.; Su, S.; Lin, M.; Meng, M.Q.H. 6-D electromagnetic tracking approach using uniaxial transmitting coil and tri-axial magneto-resistive sensor. *IEEE Sens. J.* **2017**, *18*, 1178–1186. [CrossRef]
14. Pasku, V.; De Angelis, A.; De Angelis, G.; Arumugam, D.D.; Dionigi, M.; Carbone, P.; Moschitta, A.; Ricketts, D.S. Magnetic field-based positioning systems. *IEEE Commun. Surv. Tutor.* **2017**, *19*, 2003–2017. [CrossRef]
15. Bian, S.; Hevesi, P.; Christensen, L.; Lukowicz, P. Induced Magnetic Field-Based Indoor Positioning System for Underwater Environments. *Sensors* **2021**, *21*, 2218. [CrossRef] [PubMed]
16. Sheinker, A.; Ginzburg, B.; Salomonski, N.; Frumkis, L.; Kaplan, B.Z. Localization in 3-D using beacons of low frequency magnetic field. *IEEE Trans. Instrum. Meas.* **2013**, *62*, 3194–3201. [CrossRef]
17. Feezor, M.D.; Sorrell, F.Y.; Blankinship, P.R.; Bellingham, J.G. Autonomous underwater vehicle homing/docking via electromagnetic guidance. *IEEE J. Ocean. Eng.* **2001**, *26*, 515–521. [CrossRef]
18. Peng, S.; Liu, J.; Wu, J.; Li, C.; Liu, B.; Cai, W.; Yu, H. A low-cost electromagnetic docking guidance system for micro autonomous underwater vehicles. *Sensors* **2019**, *19*, 682. [CrossRef] [PubMed]
19. Vandavasi, B.N.J.; Arunachalam, U.; Narayanaswamy, V.; Raju, R.; Vittal, D.P.; Muthiah, R.; Gidugu, A.R. Concept and testing of an electromagnetic homing guidance system for autonomous underwater vehicles. *Appl. Ocean Res.* **2018**, *73*, 149–159. [CrossRef]
20. Lin, R.; Zhao, Y.; Li, D.; Lin, M.; Yang, C. Underwater Electromagnetic Guidance Based on the Magnetic Dipole Model Applied in AUV Terminal Docking. *J. Mar. Sci. Eng.* **2022**, *10*, 995. [CrossRef]
21. Andria, G.; Attivissimo, F.; Di Nisio, A.; Lanzolla, A.M.L.; Larizza, P.; Selicato, S. Development and performance evaluation of an electromagnetic tracking system for surgery navigation. *Measurement* **2019**, *148*, 106916. [CrossRef]
22. Hu, C.; Song, S.; Wang, X.; Meng, M.Q.H.; Li, B. A novel positioning and orientation system based on three-axis magnetic coils. *IEEE Trans. Magn.* **2012**, *48*, 2211–2219. [CrossRef]
23. Gutnik, Y.; Cohen, N.; Klein, I.; Groper, M. Data-Driven Underwater Navigation workshop: AUV Close-Range Localization and Guidance Employing an Electro-Magnetic Beacon. In Proceedings of the 2023 IEEE Underwater Technology (UT), Tokyo, Japan, 6–9 March 2023; pp. 1–5.
24. Gutnik, Y.; Avni, A.; Treibitz, T.; Groper, M. On the Adaptation of an AUV into a Dedicated Platform for Close Range Imaging Survey Missions. *J. Mar. Sci. Eng.* **2022**, *10*, 974. [CrossRef]
25. Carreras, M.; Hernández, J.D.; Vidal, E.; Palomeras, N.; Ribas, D.; Ridao, P. SPARUS II AUV—A hovering vehicle for seabed inspection. *IEEE J. Ocean. Eng.* **2018**, *43*, 344–355. [CrossRef]
26. Cheng, D.K. *Field and Wave Electromagnetics*; Pearson Education India; Addison-Wesley: Boston, MA, USA, 1989.
27. Zhang, C.; Liu, H.; Ge, J.; Dong, H. FPGA-based digital lock-in amplifier with high-precision automatic frequency tracking. *IEEE Access* **2020**, *8*, 123114–123122. [CrossRef]
28. Moré, J.J. The Levenberg-Marquardt algorithm: Implementation and theory. In *Numerical Analysis*; Watson, G.A., Ed.; Springer: Berlin/Heidelberg, Germany, 1978; pp. 105–116.
29. Quigley, M.; Conley, K.; Gerkey, B.; Faust, J.; Foote, T.; Leibs, J.; Wheeler, R.; Ng, A.Y. ROS: An Open-Source Robot Operating System. In Proceedings of the ICRA Workshop on Open Source Software, Kobe, Japan, 12–17 May 2009; Volume 3, p. 5.
30. Kalaitzakis, M.; Carroll, S.; Ambrosi, A.; Whitehead, C.; Vitzilaios, N. Experimental comparison of fiducial markers for pose estimation. In Proceedings of the 2020 International Conference on Unmanned Aircraft Systems (ICUAS), Athens, Greece, 1–4 September 2020; pp. 781–789.
31. Porr, B. IIR1—Infinitely Impulse Response Filter 1. 2023. Available online: https://github.com/berndporr/iir1 (accessed on 4 January 2024).
32. Robotics, P. ArUco ROS Package. 2024. Available online: https://github.com/pal-robotics/aruco_ros (accessed on 4 January 2024).
33. Sonnaillon, M.O.; Bonetto, F.J. Lock-in amplifier error prediction and correction in frequency sweep measurements. *Rev. Sci. Instrum.* **2007**, *78*, 014701. [CrossRef] [PubMed]
34. Newman, P. Levenberg-Marquardt Algorithm with Numeric Jacobians. 2024. Available online: https://docs.mrpt.org/reference/latest/page_tutorial_math_levenberg_marquardt.html (accessed on 4 January 2024).
35. Smach, R. Python-Based Library for Hierarchical State Machines. 2024. Available online: https://wiki.ros.org/smach (accessed on 4 January 2024).

Disclaimer/Publisher's Note: The statements, opinions and data contained in all publications are solely those of the individual author(s) and contributor(s) and not of MDPI and/or the editor(s). MDPI and/or the editor(s) disclaim responsibility for any injury to people or property resulting from any ideas, methods, instructions or products referred to in the content.